Gravity Field and Internal Structure of Mercury from MESSENGER

David E. Smith*[1], Maria T. Zuber[1], Roger J. Phillips[2], Sean C. Solomon[3], Steven A. Hauck, II[4], Frank G. Lemoine[5], Erwan Mazarico[1,5], Gregory A. Neumann[5], Stanton J. Peale[6], Jean-Luc Margot[7], Catherine L. Johnson[8,9], Mark H. Torrence[10,5], Mark E. Perry[11], David D. Rowlands[5], Sander Goossens[12], James W. Head[13], Anthony H. Taylor[14]

Submitted to: *Science*
January 4, 2012

Radio tracking of the MESSENGER spacecraft has provided a model of Mercury's gravity field. In the northern hemisphere several large gravity anomalies, including one candidate mascon, exceed 100 mGal. Mercury's northern hemisphere crust is thicker at low latitudes and thinner in the polar region and shows evidence for thinning beneath some impact basins. The low-degree gravity field, combined with planetary spin parameters, yields the moment of inertia $C/MR^2 = 0.353 \pm 0.017$, where M and R are Mercury's mass and radius, and a ratio of the moment of inertia of Mercury's solid outer shell to that of the planet of $C_m/C = 0.452 \pm 0.035$. A model for Mercury¹s radial density distribution consistent with these results includes a solid silicate crust and mantle overlying a solid Fe-S layer and an Fe-rich liquid outer core and perhaps a solid inner core.

---

[1]Department of Earth, Atmospheric, and Planetary Sciences, Massachusetts Institute of Technology, Cambridge, MA 02139-4307, USA. [2]Planetary Science Directorate, Southwest Research Institute, Boulder, CO 80302, USA. [3]Department of Terrestrial Magnetism, Carnegie Institution of Washington, Washington, DC 20015, USA. [4]Department of Earth, Environmental and Planetary Sciences, Case Western Reserve University, Cleveland, OH 44106, USA. [5]NASA Goddard Space Flight Center, Greenbelt, MD 20771, USA. [6]Department of Physics, University of California, Santa Barbara, CA 93106, USA. [7]Department of Earth and Space Sciences, University of California, Los Angeles, CA 90095, USA. [8]Department of Earth and Ocean Sciences, University of British Columbia, Vancouver, BC, V6T 1Z4 Canada. [9]Planetary Science Institute, 1700 East Fort Lowell, Suite 106, Tucson, AZ 85719, USA. [10]SGT, Inc., 7701 Greenbelt Rd., Greenbelt, MD 20770, USA. [11]The Johns Hopkins University Applied Physics Laboratory, Laurel, MD 20723, USA. [12]University of Maryland, Baltimore County, Baltimore, MD 21250, USA. [13]Department of Geological Sciences, Brown University, Providence, RI 02912, USA. [14]KinetX, Inc., Tempe, AZ 85284, USA.

*To whom correspondence should be addressed: david.e.smith@nasa.gov

The internal structure of a planet preserves substantial information regarding processes that have influenced thermal and tectonic evolution, and measuring a planet's gravity field provides fundamental information for understanding a planet's internal mass distribution. Mapping Mercury's gravity field is consequently a primary objective of the MErcury Surface, Space ENvironment, GEochemistry, and Ranging (MESSENGER) mission (*1*).

On 18 March 2011, the MESSENGER spacecraft was inserted into a ~12-hour, near-polar orbit around Mercury, with an initial periapsis altitude of 200 km, initial periapsis longitude of 60°N, and apoapsis at ~15,200 km altitude in the southern hemisphere. This highly eccentric orbit permits the mapping of regional gravitational structure in the northern hemisphere at the maximum resolution of a spherical harmonic model near periapsis but limits the recoverability of the gravity field to long wavelengths at southern latitudes. At the ascending and descending nodes of the orbit (on the equator), the altitude of MESSENGER is about 4900 and 1200 km, respectively.

During the first few weeks after orbit insertion, MESSENGER was tracked extensively at X-band (8 GHz) by stations of NASA's Deep Space Network (DSN). After this initial period of nearly continuous tracking, the typical coverage was less frequent, limiting the number of direct periapsis passages that were observed. We have processed data from 18 March through 23 August 2011, a tracking period that spans more than two Mercury sidereal days (Fig. S1). We limited our analysis to one-day arcs to reduce the modeling errors from the non-conservative forces, which grow quadratically with time. The aggregated normal equations developed from daily arcs were used to develop solutions of the gravity field of Mercury (see SOM) to degree (l) and order (m) 20×20 in

spherical harmonics, a compromise between data sensitivity and global resolution. To limit the power of the high-degree coefficients because of noise in areas that lack low-altitude coverage, a Kaula power-law constraint (*2*) was applied to coefficients for spherical harmonic degrees greater than $l = 2$. That constraint ($4 \times 10^{-5}/l^2$) was derived from scaling of gravitational power for the Moon (cf. Fig. S2).

The gravity anomalies and gravitational potential (geoid) of the 20×20 spherical harmonic solution, here termed HgM002, are depicted in Figs. 1A and 1B, respectively. Projected errors derived from the covariance of the 20×20 solution are below 20 mGal north of 30°N (Fig. S3). The northern lowlands, ~2 km lower in elevation than surrounding terrain and approximately centered over the north pole (*3*), corresponds to a broad gravity low (Fig. 2). At mid-latitudes, a west-southwest–east-northeast-trending, discontinuous upland that extends for nearly half the circumference of Mercury is marked by weakly positive gravity anomalies and thus must be largely balanced at depth by thicker-than-average crust or lower-than average densities. The gravity field in the northern hemisphere shows several regional anomalies that exceed 100 mGal in amplitude. One such anomaly coincides with Mercury's northern rise, a locally elevated region (centered at 68°N, 33°E) (*3*) within the northern lowlands and north polar gravity low. Another is associated with the Caloris impact basin (35°N, 160°E), where some of the anomalous mass correlates with and can be attributed to regions of high topography on the basin floor (*3*). A third positive anomaly is associated with the Sobkou impact basin (35°N, 230°E), but the gravity anomaly is centered on the southeast rim of the basin, complicating the relation between gravity and topography. Other positive gravity anomalies are not obviously associated with mapped impact basins at the current

resolution of the gravity field. Attempts to resolve mascon anomalies similar to those seen at prominent basins on the Moon (*4*) and Mars (*5*) from tracking observations during MESSENGER's first two Mercury flybys (*6*) and the third Mariner 10 flyby (*7*) have not produced definitive results. From harmonic solution HgM002, the only identifiable mascon basin is Caloris.

The surface that represents Mercury's reference equipotential, or geoid (Fig. 1b), has a dynamic range of 200 m, and its largest anomaly is centered at Caloris. Because the spacecraft altitude over the southern hemisphere is much higher than in the northern hemisphere, the geoid error, projected from the full covariance of the HgM002 solution, is less than 20 m north of the equator but reaches 40-50 m in regions of mid to high latitudes in the southern hemisphere. The presence or absence of large geoid features in the south cannot be confirmed with the present data.

The gravity field has been combined with topography from MESSENGER's Mercury Laser Altimeter (*3*) to produce a map of the crustal thickness of Mercury's northern hemisphere (Fig. 1c). On the basis of compositional measurements (*8, 9*) from MESSENGER's X-Ray Spectrometer (XRS) indicating that the crust is intermediate between basaltic and more ultramafic compositions, as well as melting experiments on candidate mantle compositions consistent with XRS measurements (*10*), we assume a density contrast between the crust and mantle ($\Delta\rho = \rho_m - \rho_c$) of 200 kg m^{-3}. On the basis of limits determined from flyby observations of gravity and topography (*6, 11*) and constraints from tectonic models for the depth extent of faulting (*12*), we adopt a mean crustal thickness of 50 km. We also assume uniform values for the densities of the crust and mantle, and we assume that all signals in the gravity field not produced by

topography are signatures of relief on the crust-mantle boundary. The resulting map of crustal thickness (Fig. 1c) indicates that the crust is generally thicker (50-80 km) near the equator and thins toward the north polar region (20-40 km), with the regionally thinnest crust located beneath the northern lowlands (*3*). The Caloris basin overlies an area of local thinning of the crust, consistent with the interpretation of mascon basins on the Moon (*13*) and Mars (*14*) that crustal thinning beneath basins contributes substantially to the observed gravity anomaly.

A comparison of gravity anomalies that would result from Mercury's shape alone with the gravity anomalies from the HgM002 solution is made in Fig. 2. High-standing terrain borders many parts of the northern lowlands (*3*), as is also evident in the broader-scale view here of the corresponding gravity field (Fig. 2A). Mild gravity anomalies associated with this terrain (Fig. 2B) suggest a high degree of interior mass compensation. By contrast, the northern rise has a gravity anomaly nearly as strong as that due to shape alone (~150 versus ~170 mGal), indicating little mass compensation and a thick lithosphere. We have estimated the thickness, T_e, of the effective elastic lithosphere beneath the northern rise by assuming that partial compensation takes place at the crust-mantle boundary and then finding model solutions that best fit the gravity anomaly in terms of crustal and elastic lithosphere thicknesses (see SOM). Over a crustal thickness range of 25–100 km, T_e is 70–90 km, and the downward flexural deflection of the crust-mantle boundary is minor (3-5 km), consistent with the lack of a discernable crustal thickness anomaly at the northern rise (Fig. 1C). An elastic lithosphere is a surrogate for one with more complex temperature-dependent strength, but temperatures in the crust and uppermost mantle vary approximately inversely with T_e. The northern

rise, part of the northern smooth plains volcanic complex (*15*), has been estimated from its impact crater size-frequency distribution to have a surface that formed ~3.7-3.8 billion years ago (Ga), substantially younger than that of the surrounding heavily cratered highlands (*16*). The greater level of apparent mass compensation of the highlands will yield, under similar assumptions, a thinner elastic lithosphere and higher crustal and mantle temperatures at the time of formation than the northern rise. The inference that Mercury's interior generally cooled with time is in keeping thermal evolution models for the terrestrial planets. T_e estimates for Mars derived from gravity-topography relations for regions with ages of major topographic features similar to that of the northern rise, in contrast, are considerably smaller (*17*).

The major parameters of gravity field solution HgM002, including the product of the gravitational constant and Mercury's mass (*GM*) and the normalized low-degree coefficients along with their standard errors, are given in Table 1. The *GM* value is close to that given by the most recent previous model of Mercury's gravitational field (HgM001), derived solely from the tracking of MESSENGER during its first two near-equatorial flybys (*6*).

The covariance matrix of solution HgM002 was used to generate clone models of the gravity field in order to analyze the error characteristics for the degree-2 coefficients and C_{30} (see SOM). The distributions of admissible coefficient values are depicted in Fig. S5 for the degree-2 coefficients. C_{20} and C_{22} are tightly bounded with small relative uncertainties, and C_{21} and S_{21} are small as expected (see Table 1).

The C_{20} and C_{22} terms provide important constraints on the interior structure of Mercury because they are directly relatable to the radial distribution of density. Earth-

based radar measurements of Mercury's orientation and rotation (*18*) confirmed that the planet occupies a Cassini state in which the axis of rotation is nearly perpendicular to the orbital plane and the spin and orbital precession rates are equal. This state allows the determination of Mercury's normalized polar moment of inertia, C/MR^2, where R is Mercury's mean radius, and a measurement of the ratio of the polar moment of inertia C_m of the solid outer portion of the planet (*6, 18*) to that of the entire planet (*19, 20*). The values of C_{20} and C_{22} (Table 1) combined with Earth-based radar measurements of the amplitude of Mercury's forced libration and obliquity (*18*), and ancillary data on the precession rate and pole position (*21*) provide the information necessary to estimate C/MR^2 and C_m/C. A libration amplitude of 35.8 ± 2 arcseconds and a slightly revised obliquity value of 2.06 ± 0.1 arcmin (*22*) yields internal structure parameters C/MR^2 = 0.353 ± 0.0172 and C_m/C = 0.454 ± 0.0353.

The C/MR^2 and C_m/C values provide the strongest constraints yet on the internal layering of Mercury. Fig. 3 shows the resulting moment of inertia parameters for more than one million Monte Carlo models that include a silicate crust and mantle as well as an Fe-rich core that may contain solid and liquid layers. These models are constrained only by the mean radius (2440 km) and bulk density of Mercury (5430 kg m^{-3}) (e.g., *23*). Comparison of the internal structure models with the measured moment inertia parameters indicates that the outer radius of the liquid portion of the core under the adopted modeling assumptions is 2030 ± 37 km (1 standard deviation), and the density of the outer shell overlying the liquid core is 3650 ± 225 kg m^{-3}. The procedure does not provide a size estimate for any solid inner component of the core.

The large average bulk density inferred for Mercury's solid outer shell is surprising given that measurements by the MESSENGER XRS determined an upper bound on the average surface abundance of Fe of ~ 4 wt % (*8*). Although uncertainty in the density of the solid shell permits a wide range of possibilities, the nominal value provides an important constraint on the planet's bulk composition. The low Fe abundance in volcanic rocks at Mercury's surface suggests Mercury's silicate mantle is also low in iron and cannot account for the outer shell density. Relatively low surface abundances of Ti and Al (*8*) are also inconsistent with substantial amounts of such high-density mantle minerals as ilmenite and garnet. A deeper reservoir of high-density material is therefore needed to account for the large solid-shell density and moment of inertia. One possibility is a dense silicate layer, possibly Fe-bearing, that has not substantively participated in the generation of Mercury's crust.

Alternatively, Mercury may have a solid layer of FeS at the top of the core. The highly reducing chemical conditions implied for Mercury's precursory materials by the low Fe and high S content of surface rocks (*8*) suggest that Mercury's core likely contains substantial Si as well as S. Fe-S-Si alloys are subject to liquid immiscibility at pressures less than ~15 GPa (*24*), resulting in the buoyancy segregation of S-rich liquids at the top of the core. The density of solid FeS is sufficiently low that for a broad range of conditions the solid form would likely remain at the top of the core. There is a strong, albeit poorly constrained, trade-off between the thickness of a basal solid FeS layer and the density of the silicate mantle, though the basal layer could be a few tens of kilometers to as much as ~200 km in thickness. The thickness of the outer silicate portion of the planet would, under this interpretation, be thinner than the nominal 410 km depth to the

solid-liquid boundary. A solid FeS layer at the base of the mantle would place strong constraints on the present thermal structure of Mercury. Moreover, a static, electrically conducting layer at the top of the core would act to decrease the overall strength of the field observable at or above the planetary surface and would attenuate harmonic components of the magnetic field increasingly strongly with increasing degree (*25*).

The gravity field results point to a much different interior structure for Mercury from that heretofore anticipated and from those of the other terrestrial planets. Further measurements and additional models of interior dynamics and evolution should enable a fuller exploration of the extent to which this new view of Mercury's interior structure may be relatable to similarly surprising evidence from MESSENGER observations of Mercury's surface for widespread, high-temperature volcanism *(15)*; long-wavelength modification of surface topography (*3*); and tectonic activity over an extended period of Mercury's geologic history (*26*).

References and Notes

1. S. C. Solomon, R. L. McNutt, Jr., R. E. Gold, D. L. Domingue, MESSENGER mission overview. *Space Sci. Rev.* **131**, 3 (2007).
2. W. M. Kaula, *Theory of Satellite Geodesy*. (Blaisdell, Waltham, 1966), 124 pp.
3. M. T. Zuber *et al.*, Topography of the northern hemisphere of Mercury from MESSENGER laser altimetry. *Science*, submitted (2012).
4. P. M. Muller, W. L. Sjogren, Mascons: Lunar mass concentrations. *Science* **161**, 680 (1968).
5. D. E. Smith *et al.*, An improved gravity model for Mars: Goddard Mars Model-1 (GMM-1). *J. Geophys. Res.* **98**, 20 (1993).
6. D. E. Smith *et al.*, The equatorial shape and gravity field of Mercury from MESSENGER flybys 1 and 2. *Icarus* **209**, 247 (2010).
7. J. Palguta, J. D. Anderson, G. Schubert, Constraining the location and dimensions of mass anomalies on Mercury from Mariner 10 Doppler data. *J. Geophys. Res.*, submitted (2011).
8. L. R. Nittler *et al.*, The major-element composition of Mercury's surface from MESSENGER X-ray spectrometry. *Science* **333**, 1847 (2011).
9. L. R. Nittler *et al.*, Major elements on Mercury's surface from MESSENGER X-ray spectrometry, paper presented at the Geol. Soc. Am. Annual Meeting, Minneapolis, MN, 9-12 October 2011.
10. B. Charlier, T. L. Grove, M. T. Zuber, Composition and differentiation of "basalts" at the surface of Mercury. *Lunar Planet. Sci.,* **53**, submitted (2012).
11. M. T. Zuber *et al.*, Laser altimeter observations from MESSENGER's first Mercury flyby. *Science* **321**, 77 (2008).

12. F. Nimmo, T. R. Watters, Depth of faulting on Mercury: Implications for heat flux and crustal and effective elastic thickness. *Geophys. Res. Lett.* **31**, L02701, doi:10.1029/2003GL018847 (2004).
13. G. A. Neumann, M. T. Zuber, D. E. Smith, F. G. Lemoine, The lunar crust: Global signature and structure of major basins. *J. Geophys. Res.* **101**, 16841 (1996).
14. M. T. Zuber *et al.*, Internal structure and early thermal evolution of Mars from Mars Global Surveyor topography and gravity. *Science* **287**, 1788 (2000).
15. J. W. Head *et al.*, Flood volcanism in the northern high latitudes of Mercury revealed by MESSENGER. *Science* **333**, 1853 (2011).
16. R. G. Strom, G. A. Neukum, in *Mercury,* C. R. Chapman, F. Villas, M. S. Matthews, Eds. (Univ. Ariz. Press, Tucson, AZ, 1988), pp. 363-373.
17. P. J. McGovern *et al.*, Correction to "Localized gravity/topography admittances and correlation spectra on Mars: Implications for regional and global evolution". *J. Geophys. Res.* **109**, E07007, doi:10.1029/2004JE002286 (2004).
18. J.-L. Margot, S. J. Peale, R. F. Jurgens, M. A. Slade, I. V. Holin, Large longitude libration of Mercury reveals a molten core. *Science* **316**, 710 (2007).
19. S. J. Peale, Does Mercury have a molten core? *Nature* **262**, 765 (1976).
20. S. J. Peale, R. J. Phillips, S. C. Solomon, D. E. Smith, M. T. Zuber, A procedure for determining the nature of Mercury's core. *Meteorit. Planet. Sci.* **37**, 1269 (2002).
21. M. Yseboodt, J.-L. Margot, Evolution of Mercury's obliquity. *Icarus* **181**, 327 (2006).
22. J.-L. Margot, S. Padovan, S. J. Peale, S. C. Solomon, Measurements of Mercury's spin state and inferences about its interior. paper presented at the Amer. Geophys. Un. Fall Meeting, San Francisco, CA, 9-12 December 2011.
23. S. A. Hauck, II, S. C. Solomon, D. A. Smith, Predicted recovery of Merury's internal structure by MESSENGER. *Geophys. Res. Lett.* **34**, L18201, doi:10.1029/2007GL030793 (2007).
24. G. Morard, T. Katsura, Pressure-temperature cartography of Fe-S-Si immiscible system. *Geochim. Cosmochim. Acta* **74**, 3659 (2010).
25. U. Christensen, A deep dynamo generating Mercury's magnetic field. *Nature* **444**, 1056 (2006).
26. M. T. Zuber *et al.*, Lithospheric strain accommodation on Mercury from altimetric profiles of ridges and lobate scarps measured during MESSENGER flybys 1 and 2. *Icarus* **209**, 88 (2010).
27. D. E. Pavlis, S. G. Poulouse, J. J. McCarthy, “GEODYN Operations Manuals” (SGT, Inc., Greenbelt, MD, 2009).
28. J.-L. Margot, A Mercury orientation model including non-zero obliquity and libration. *Celestial Mech. Dyn. Astron.* **105**, 329 (2009).
29. R. E. Ulman, “SOLVE Program: Mathematical Formulation and Guide to User Input” (Hughes/STX Contractor Report, contract NAS5-31760, 1994).
30. E. Mazarico, F. G. Lemoine, S.-C. Han, D. E. Smith, GLGM-3, a degree-150 lunar gravity model fom the historical tracking data of NASA Moon orbiters. *J. Geophys. Res.* **115**, E05001, doi:10.1029/2009JE003472 (2010).
31. F. G. Lemoine *et al.*, An improved solution of the gravity field of Mars (GMM-2B) from Mars Global Surveyor. *J. Geophys. Res.* **106**, 23,359 (2001).
32. J. A. Marshall, S. B. Lutchke, Modeling radiation forces acting on TOPEX/Poseidon for precision orbit determination. *J. Spacecraft Rockets* **31**, 99 (1994).
33. D. L. Turcotte, R. J. Willemann, W. F. Haxby, J. Norberry, Role of membrane stresses in the support of planetary topography. *J. Geophys. Res.* **86**, 3951 (1981).
34. The MESSENGER project is supported by the NASA Discovery Program under contracts NAS5-97271 to The Johns Hopkins University Applied Physics Laboratory and NASW-00002 to the Carnegie Institution of Washington. We acknowledge the contributions of the MESSENGER spacecraft team and the radio science and MLA instrument teams in acquiring the observations used herein.

04 January 2012

Table 1. Normalized low-degree gravity coefficients in the HgM002 gravity model for Mercury.

Parameter	Value	Uncertainty	Comments
GM, $km^3\ s^{-2}$	22031.780	± 0.02	No significant difference from HgM001.
$C_{20} \times 10^{-5}$	-2.25	± 0.01	~20% smaller than Mariner 10 estimate of $(-2.68 \pm 0.89) \times 10^{-5}$.
$C_{21} \times 10^{-8}$	-4.64	± 5	Consistent with co-alignment of gravity field and angular momentum vector.
$S_{21} \times 10^{-8}$	1.35	± 5	
$C_{22} \times 10^{-5}$	1.253	± 0.01	Ratio of S_{22}/C_{22} is small, indicating that the equatorial major axis of the gravity field is
$S_{22} \times 10^{-5}$	0.005	± 0.01	aligned with Mercury's "hot-pole" longitudes.
$C_{30} \times 10^{-6}$	-4.49	± 0.3	Negative value indicates that a periapsis over the south pole is needed for a stable spacecraft orbit about Mercury.
$C_{40} \times 10^{-6}$	-6.5	± 0.8	

Figure Captions

Figure 1. Maps of Mercury's (**A**) free-air gravity anomaly**,** (**B**) geoid anomaly, and (**C**) crustal thickness (cylindrical projections). The height of the geoid anomaly is calculated with respect to an ellipsoid given by the rotational and degree-2 zonal gravity potential for which the average radius at the equator is 2440 km. The potential on the geoid is the sum of the even zonal harmonics in the potential to degree 20 and the rotational potential, under the convention that potential increases outward. The reference potential is $9.02956464 \times 10^6\ m^2\ s^{-2}$. In the crustal thickness map, the shaded area indicates a lack of MLA altimetry (*3*) and weak gravity anomalies due to high spacecraft altitude (see Fig. S1).

Figure 2. (**A**) The radial component of the gravitational acceleration vector resulting from a 20 × 20 spherical harmonic expansion of Mercury's shape (*3*) given a density of upper crustal material of 3100 kg m^{-3}. Results are shown in a polar stereographic projection north of 40°N. "NR" indicates the location of the northern rise. (**B**) The radial component of the gravitational acceleration vector resulting from the 20 × 20 HgM002 spherical harmonic gravity solution. In both plots, the solution shown has been limited to spherical harmonic terms with degrees 6 and greater to emphasize local- to regional-scale anomalies.

Figure 3. (**A**) Outer radius of Mercury's liquid core. (**B**) Average density of the solid shell that overlies the liquid core. The stars represent the central values for C/MR^2 and C_m/C, and the black bars denote ± one standard deviation.

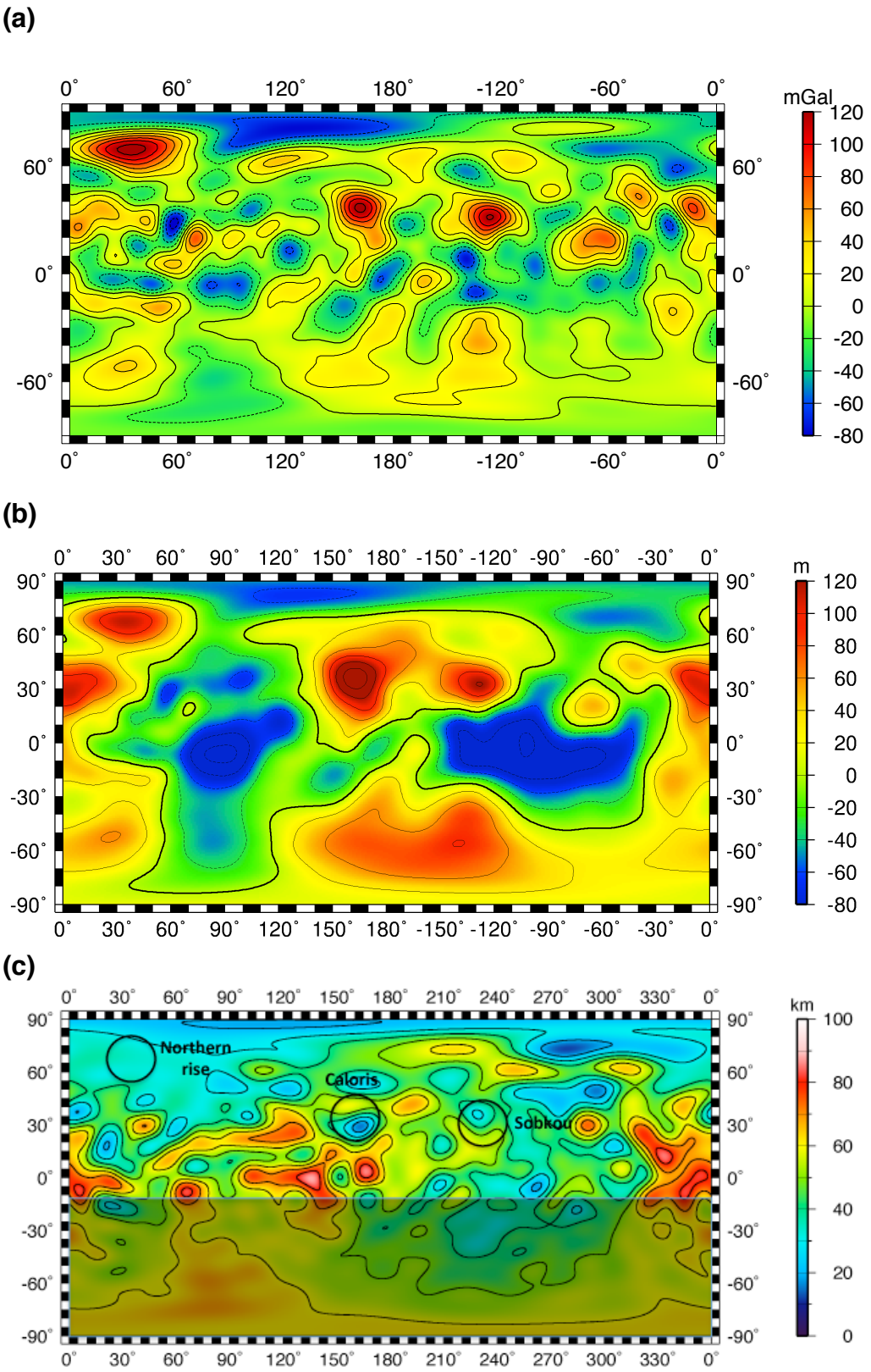

Figure 1
Smith et al.

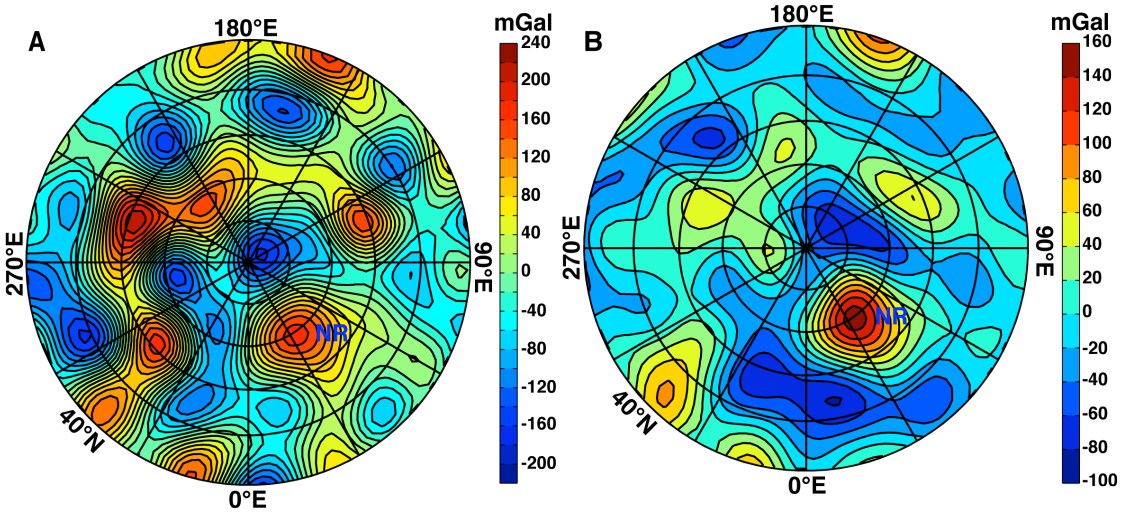

Figure 2
Smith et al.

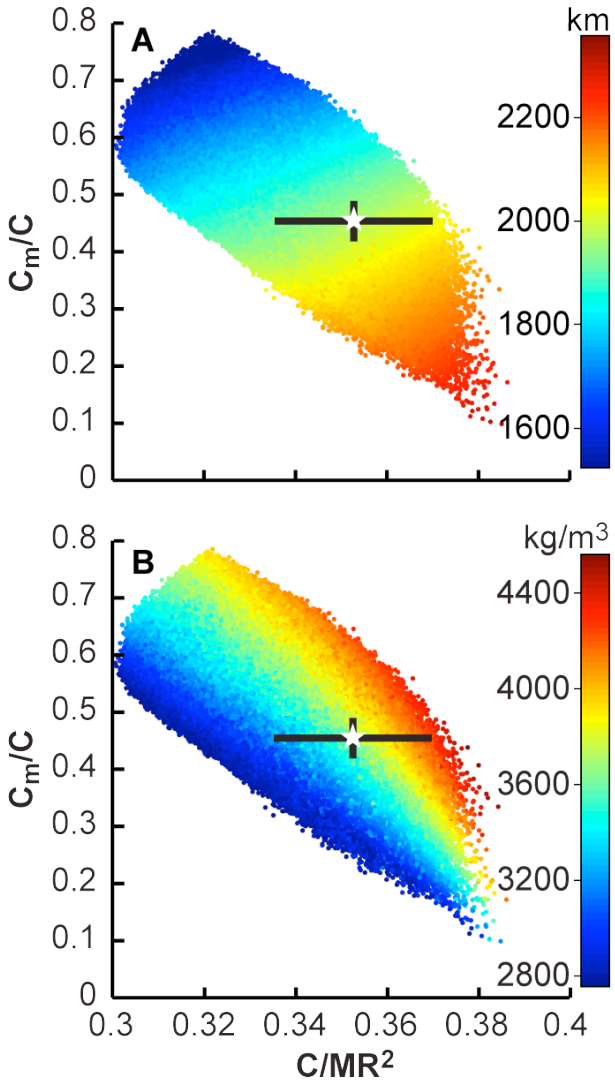

Figure 3
Smith et al.

Gravity Field and Internal Structure of Mercury from MESSENGER

David E. Smith*[2], Maria T. Zuber[1], Roger J. Phillips[2], Sean C. Solomon[3], Steven A. Hauck, II[4], Frank G. Lemoine[5], Erwan Mazarico[1,5], Gregory A. Neumann[5], Stanton J. Peale[6], Jean-Luc Margot[7], Catherine L. Johnson[8,9], Mark H. Torrence[10,5], Mark E. Perry[11], David D. Rowlands[5], Sander Goossens[12], James W. Head[13], Anthony H. Taylor[14]

Supporting Online Material

Method of Solution

The HgM002 20 × 20 harmonic solution for Mercury's gravity field used 129 daily orbital arcs, shown in Fig. S1, derived from X-band Doppler tracking of the MESSENGER spacecraft during the period 18 March to 23 August 2011. The solution also included X-band Doppler data from the first two MESSENGER flybys (designated M1 and M2) of Mercury (*6*). A total of 1.2 million observations contributed to this solution.

Processing of Deep Space Network (DSN) data from MESSENGER was accomplished using the NASA Goddard Space Flight Center (GSFC) Orbit Determination and Geodetic Parameter Estimation Program (GEODYN) (*27*). The planetary orientation model (*28*) incorporated values of Mercury's physical and rotational parameters including the longitudinal librations. When the data were processed in daily (24-h) arcs, the typical fit to the Doppler data had residuals of ~0.4 ± 0.2 mm s^{-1}, several times the noise level of the DSN data (~0.1 mm s^{-1}). We excluded tracking observations closest to superior conjunction in these solutions. Once normal equations were obtained by the GEODYN program, solutions for Mercury's gravity field were obtained via

[2]Department of Earth, Atmospheric, and Planetary Sciences, Massachusetts Institute of Technology, Cambridge, MA 02139-4307, USA. [2]Planetary Science Directorate, Southwest Research Institute, Boulder, CO 80302, USA. [3]Department of Terrestrial Magnetism, Carnegie Institution of Washington, Washington, DC 20015, USA. [4]Department of Earth, Environmental and Planetary Sciences, Case Western Reserve University, Cleveland, OH 44106, USA. [5]NASA Goddard Space Flight Center, Greenbelt, MD 20771, USA. [6]Department of Physics, University of California, Santa Barbara, CA 93106, USA. [7]Department of Earth and Space Sciences, University of California, Los Angeles, CA 90095, USA. [8]Department of Earth and Ocean Sciences, University of British Columbia, Vancouver, BC, V6T 1Z4 Canada. [9]Planetary Science Institute, 1700 East Fort Lowell, Suite 106, Tucson, AZ 85719, USA. [10]SGT, Inc., 7701 Greenbelt Rd., Greenbelt, MD 20770, USA. [11]The Johns Hopkins University Applied Physics Laboratory, Laurel, MD 20723, USA. [12]University of Maryland, Baltimore County, Baltimore, MD 21250, USA. [13]Department of Geological Sciences, Brown University, Providence, RI 02912, USA. [14]KinetX, Inc., Tempe, AZ 85284, USA.

*To whom correspondence should be addressed: david.e.smith@nasa.gov

NASA GSFC SOLVE software (*29*) in a fashion similar to those used for gravity field solutions for the Moon (*30)* and Mars (*31*).

In constructing solutions for the gravitational field, the orbit and data modeling accounted for solar radiation pressure, planetary radiation pressure induced by the reflected solar and thermal radiation from the planet Mercury, third-body gravity perturbations from the Sun and other planets, and relativistic corrections including the modification of the central body term in the force model and light-time effects in the measurement model. A mean planetary albedo of 0.074 and the planetary thermal model derived by D. A. Paige (personal communication, 2011) were used. The tracking data were corrected for DSN station coordinate effects, including Earth's polar motion, solid-Earth tides, and ocean loading. Meteorological data at the stations were used to correct the radiometric tracking data for propagation effects through Earth's troposphere.

The modeling included a box-wing representation of the MESSENGER probe that approximates the spacecraft as a series of flat plates with specific cross-sectional areas and specular and diffuse reflectivities. The plates were oriented in space by means of the spacecraft attitude data (quaternions) (*32*).

MESSENGER does not have a steerable high-gain antenna (as, for example, on the Mars Reconnaissance Orbiter) but relies on six separate antennae mounted on different faces of the spacecraft, each with a distinct offset with respect to the center of mass of the spacecraft. The processing of the tracking data accounted for the routine switching among the different antennae, for which the schedule of use for tracking varies by day and mission phase. Each of the offsets of the MESSENGER tracking antennae from the spacecraft center of mass was explicitly modeled.

Given the temporal span of the data and Mercury's low spin rate, we did not solve for the solid-planet tidal Love number but rather used a fixed value ($k_2 = 0.2$). The solid-planet tide can alias into our recovery of the gravitational flattening, C_{20}, but that contribution is expected to be very small (~0.001 C_{20}), which we confirmed by obtaining an alternative solution with a different *a priori* value of k_2 (= 0.6).

The MESSENGER navigation team conducted an independent analysis and produced an independent solution for Mercury's gravity field using MESSENGER orbital tracking data through 5 October 2011. The Doppler observations were processed using the JPL MIRAGE software, and the solution agrees closely with HgM002 with respect to the values of the degree-2 terms and the pattern of gravity anomalies in the Northern Hemisphere.

Analysis of the Gravitational Field

The power in the gravitational field, expressed as RMS power, is given in Fig. S2, and gravity anomaly errors are given in Fig. S3. Correlations between low-degree coefficients are shown in Fig. S4. The correlation matrix indicates that zonal coefficients exhibit higher intra-order correlations than tesseral or sectoral coefficients, with the highest correlation between C_{20} and C_{30}. The first two MESSENGER flybys of Mercury were valuable in constraining GM, the product of the gravitational constant G and Mercury's mass M, and reducing its correlation with C_{20}.

To better understand the error characteristics of the low-degree field, the HgM002 covariance matrix was used to generate clone models and to analyze the distribution of spherical harmonic coefficients. To generate a clone gravity model, the covariance matrix

was diagonalized. Subsequently, each eigenvector was multiplied by ±1 times the square root of its eigenvalue in a random fashion, and the difference coefficients of the field were generated. More than 50000 clone models were evaluated (cf. Fig. S5).

Relations between perturbed and non-perturbed values of the C_{20} and C_{22} coefficients are plotted in Fig. S6. We processed the MESSENGER Doppler data from 19 March to 5 June 2011 simultaneously with approximately 2700 altimeter crossovers derived from MESSENGER's Mercury Laser Altimeter (MLA) (*3*). The root-mean-square (RMS) fit to the altimeter crossovers (which were not included in the orbit solution) with HgM002 is about 80 m. Fig. S6 shows that if the C_{20} and C_{22} values are perturbed by ±10 percent, the altimeter crossover RMS fit degrades to 180–230 m. This test provides a strong validation of the values for C_{20} and C_{22} obtained with the HgM002 solution.

Gravity Modeling

We generated model gravity predictions to compare with the HgM002 solution by calculating the "degree of compensation" (*33*), a calculation that employs a spherical harmonic formalism to describe the flexural and membrane response to a surface load (e.g., shape) for which some level of compensation takes place at the crust-mantle boundary. The degree of compensation was folded into the isostatic response function, which maps shapes of the surface and crust-mantle boundaries into the model gravity predications. Parameters in the model are the Young's modulus (100 GPa) and Poisson's ratio (0.25) of the elastic lithosphere, crustal density (3100 kg m^{-3}), mantle density (3300 kg m^{-3}), reference crustal thickness (h_c, variable), and thickness of the elastic lithosphere (T_e, variable). The h_c-T_e parameter space was searched for model gravity solutions that best fit the HgM002 gravity solution in the vicinity of Mercury's northern rise. Best-fitting solutions (Fig. S7) had fit standard deviations of 7 mGal (cf. the peak gravity anomaly for the northern rise is ~150 mGal), and the variance of the northern-rise gravity anomaly was reduced 99.7% by the models. The 70-90 km range found for T_e will lead to a small curvature of the load-induced deflection, so the thickness of the mechanical lithosphere (the outermost shell of the planet displaying long-term strength) will be approximately that of the elastic lithosphere.

References and Notes

1. S. C. Solomon, R. L. McNutt, Jr., R. E. Gold, D. L. Domingue, MESSENGER mission overview. *Space Sci. Rev.* **131**, 3 (2007).
2. W. M. Kaula, *Theory of Satellite Geodesy*. (Blaisdell, Waltham, 1966), 124 pp.
3. M. T. Zuber *et al.*, Topography of the northern hemisphere of Mercury from MESSENGER laser altimetry. *Science*, submitted (2012).
4. P. M. Muller, W. L. Sjogren, Mascons: Lunar mass concentrations. *Science* **161**, 680 (1968).
5. D. E. Smith *et al.*, An improved gravity model for Mars: Goddard Mars Model-1 (GMM-1). *J. Geophys. Res.* **98**, 20 (1993).
6. D. E. Smith *et al.*, The equatorial shape and gravity field of Mercury from MESSENGER flybys 1 and 2. *Icarus* **209**, 247 (2010).
7. J. Palguta, J. D. Anderson, G. Schubert, Constraining the location and dimensions of mass anomalies on Mercury from Mariner 10 Doppler data. *J. Geophys. Res.*, submitted (2011).
8. L. R. Nittler *et al.*, The major-element composition of Mercury's surface from MESSENGER X-ray spectrometry. *Science* **333**, 1847 (2011).

9. L. R. Nittler *et al.*, Major elements on Mercury's surface from MESSENGER X-ray spectrometry, paper presented at the Geol. Soc. Am. Annual Meeting, Minneapolis, MN, 9-12 October 2011.
10. B. Charlier, T. L. Grove, M. T. Zuber, Composition and differentiation of "basalts" at the surface of Mercury. *Lunar Planet. Sci.,* **53**, submitted (2012).
11. M. T. Zuber *et al.*, Laser altimeter observations from MESSENGER's first Mercury flyby. *Science* **321**, 77 (2008).
12. F. Nimmo, T. R. Watters, Depth of faulting on Mercury: Implications for heat flux and crustal and effective elastic thickness. *Geophys. Res. Lett.* **31**, L02701, doi:10.1029/2003GL018847 (2004).
13. G. A. Neumann, M. T. Zuber, D. E. Smith, F. G. Lemoine, The lunar crust: Global signature and structure of major basins. *J. Geophys. Res.* **101**, 16841 (1996).
14. M. T. Zuber *et al.*, Internal structure and early thermal evolution of Mars from Mars Global Surveyor topography and gravity. *Science* **287**, 1788 (2000).
15. J. W. Head *et al.*, Flood volcanism in the northern high latitudes of Mercury revealed by MESSENGER. *Science* **333**, 1853 (2011).
16. R. G. Strom, G. A. Neukum, in *Mercury,* C. R. Chapman, F. Villas, M. S. Matthews, Eds. (Univ. Ariz. Press, Tucson, AZ, 1988), pp. 363-373.
17. P. J. McGovern *et al.*, Correction to "Localized gravity/topography admittances and correlation spectra on Mars: Implications for regional and global evolution". *J. Geophys. Res.* **109**, E07007, doi:10.1029/2004JE002286 (2004).
18. J.-L. Margot, S. J. Peale, R. F. Jurgens, M. A. Slade, I. V. Holin, Large longitude libration of Mercury reveals a molten core. *Science* **316**, 710 (2007).
19. S. J. Peale, Does Mercury have a molten core? *Nature* **262**, 765 (1976).
20. S. J. Peale, R. J. Phillips, S. C. Solomon, D. E. Smith, M. T. Zuber, A procedure for determining the nature of Mercury's core. *Meteorit. Planet. Sci.* **37**, 1269 (2002).
21. M. Yseboodt, J.-L. Margot, Evolution of Mercury's obliquity. *Icarus* **181**, 327 (2006).
22. J.-L. Margot, S. Padovan, S. J. Peale, S. C. Solomon, Measurements of Mercury's spin state and inferences about its interior. paper presented at the Amer. Geophys. Un. Fall Meeting, San Francisco, CA, 9-12 December 2011.
23. S. A. Hauck, II, S. C. Solomon, D. A. Smith, Predicted recovery of Merury's internal structure by MESSENGER. *Geophys. Res. Lett.* **34**, L18201, doi:10.1029/2007GL030793 (2007).
24. G. Morard, T. Katsura, Pressure-temperature cartography of Fe-S-Si immiscible system. *Geochim. Cosmochim. Acta* **74**, 3659 (2010).
25. U. Christensen, A deep dynamo generating Mercury's magnetic field. *Nature* **444**, 1056 (2006).
26. M. T. Zuber *et al.*, Lithospheric strain accommodation on Mercury from altimetric profiles of ridges and lobate scarps measured during MESSENGER flybys 1 and 2. *Icarus* **209**, 88 (2010).
27. D. E. Pavlis, S. G. Poulose, J. J. McCarthy, “GEODYN Operations Manuals” (SGT Inc., Greenbelt MD, 2009).
28. J.-L. Margot, A Mercury orientation model including non-zero obliquity and libration. *Celestial Mech. Dyn. Astron.* **105**, 329 (2009).
29. R. E. Ulman, “SOLVE Program: Mathematical Formulation and Guide to User Input” (Hughes/STX Contractor Report, contract NAS5-31760, 1994).
30. E. Mazarico, F. G. Lemoine, S.-C. Han, D. E. Smith, GLGM-3, a degree-150 lunar gravity model fom the historical tracking data of NASA Moon orbiters. *J. Geophys. Res.* **115**, E05001, doi:10.1029/2009JE003472 (2010).
31. F. G. Lemoine *et al.*, An improved solution of the gravity field of Mars (GMM-2B) from Mars Global Surveyor. *J. Geophys. Res.* **106**, 23,359 (2001).
32. J. A. Marshall, S. B. Luthke, Modeling radiation forces acting on TOPEX/Poseidon for precision orbit determination. *J. Spacecraft Rockets* **31**, 99 (1994).

33. D. L. Turcotte, R. J. Willemann, W. F. Haxby, J. Norberry, Role of membrane stresses in the support of planetary topography. *J. Geophys. Res.* **86**, 3951 (1981).
34. The MESSENGER project is supported by the NASA Discovery Program under contracts NAS5-97271 to The Johns Hopkins University Applied Physics Laboratory and NASW-00002 to the Carnegie Institution of Washington. We acknowledge the contributions of the MESSENGER spacecraft team and the radio science and MLA instrument teams in acquiring the observations used herein.

FIGURE CAPTIONS

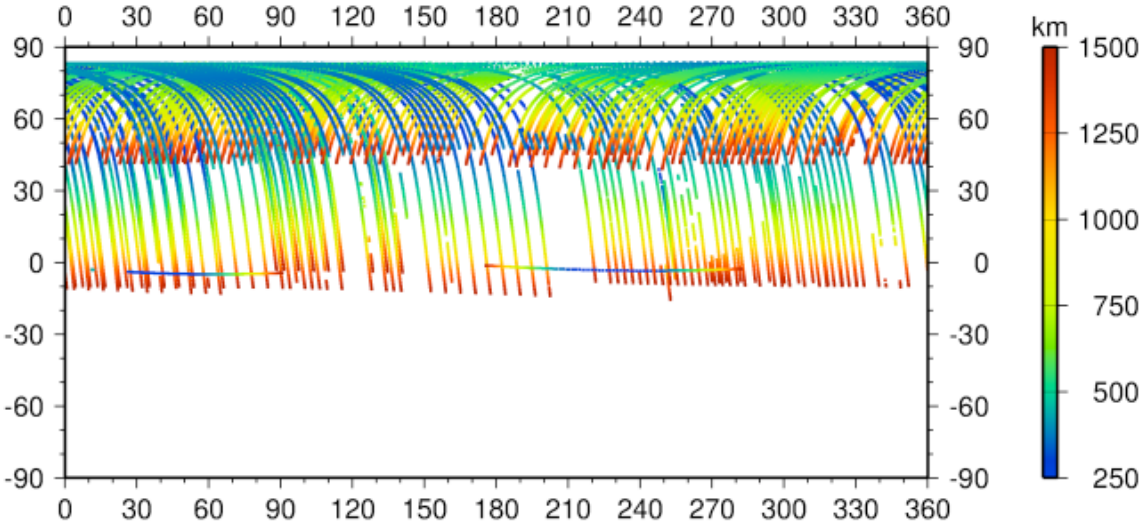

Figure S1. Distribution of Doppler tracking data acquired when the MESSENGER spacecraft was within 1500-km altitude of the surface of Mercury (cylindrical projection). Color coding indicates spacecraft altitude.

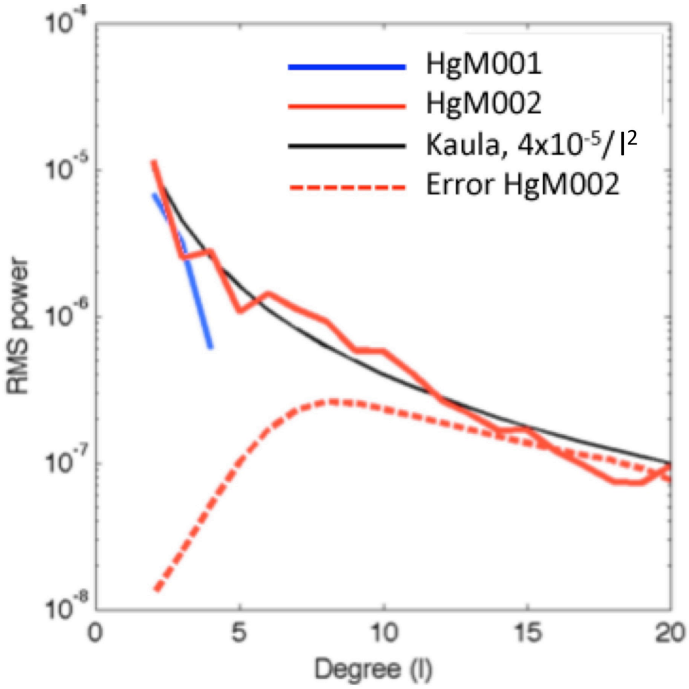

Figure S2. RMS power for solution HgM002. Variances for earlier solution HgM001 (*6*) are also shown, as are the adopted Kaula constraint (*2*) and the errors in solution HgM002 by harmonic degree.

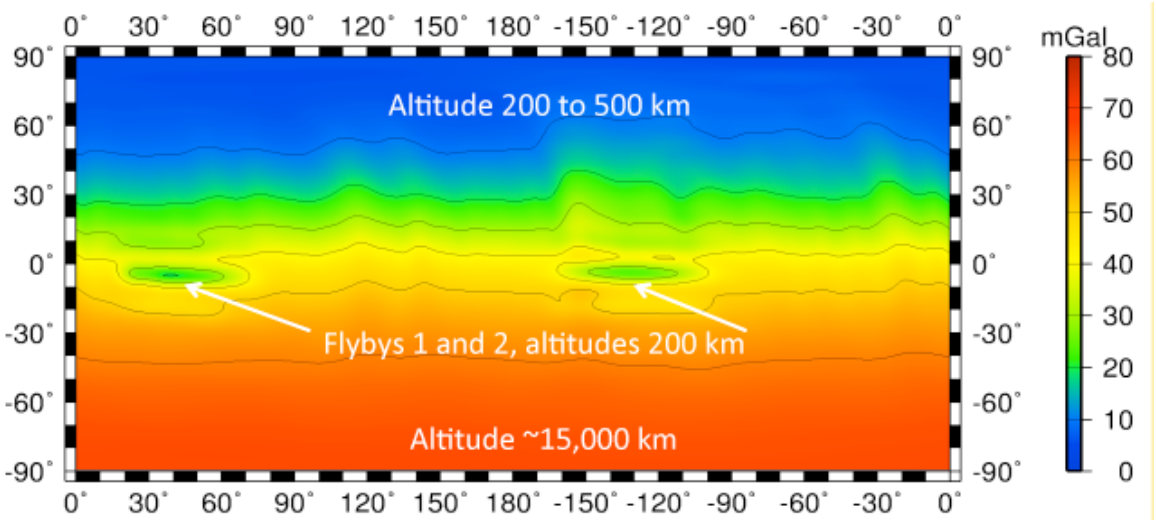

Figure S3. Cylindrical projection of gravity anomaly errors for solution HgM002.

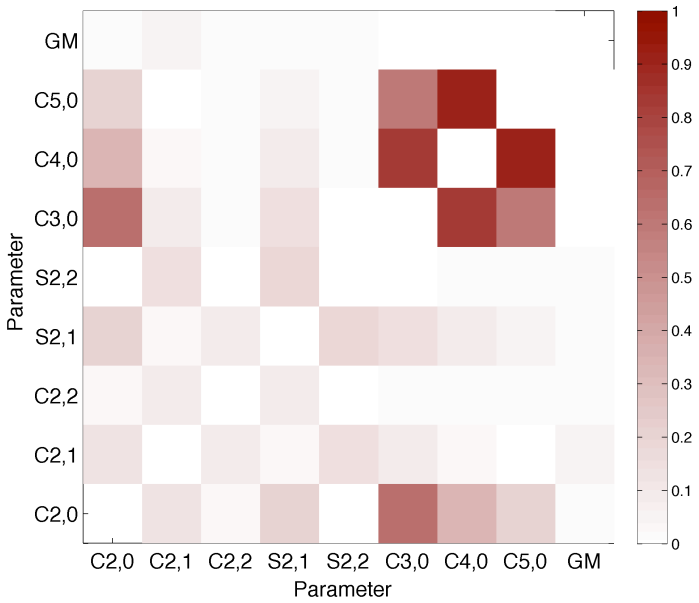

Figure S4. Correlation matrix for *GM* and the low-degree harmonic coefficients in the HgM002 solution.

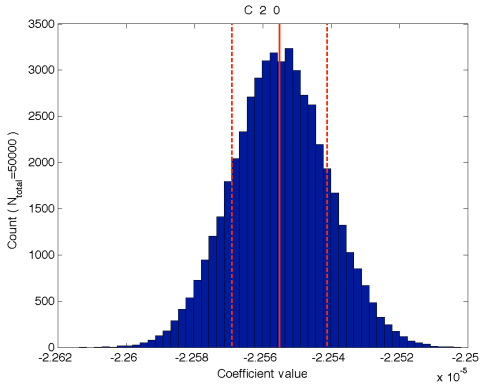
C 2 0
Count (N_total=50000)
Coefficient value
x 10^-5

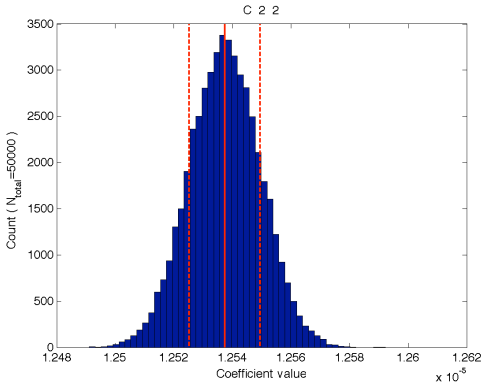
C 2 2
Count (N_total=50000)
Coefficient value
x 10^-5

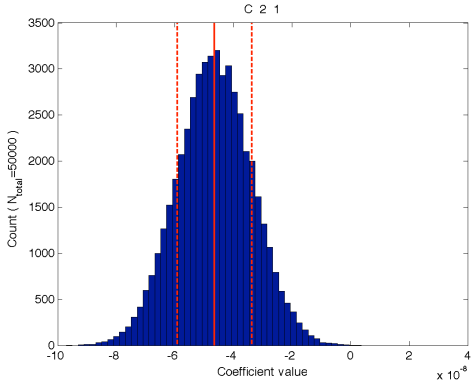
C 2 1
Count (N_total=50000)
Coefficient value
x 10^-8

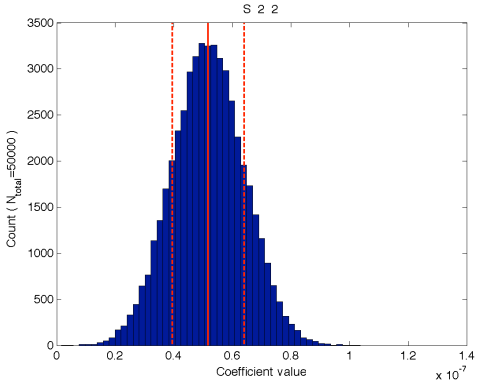
S 2 2
Count (N_total=50000)
Coefficient value
x 10^-7

Figure S5. Distribution of selected coefficient values from the analysis of clone models.

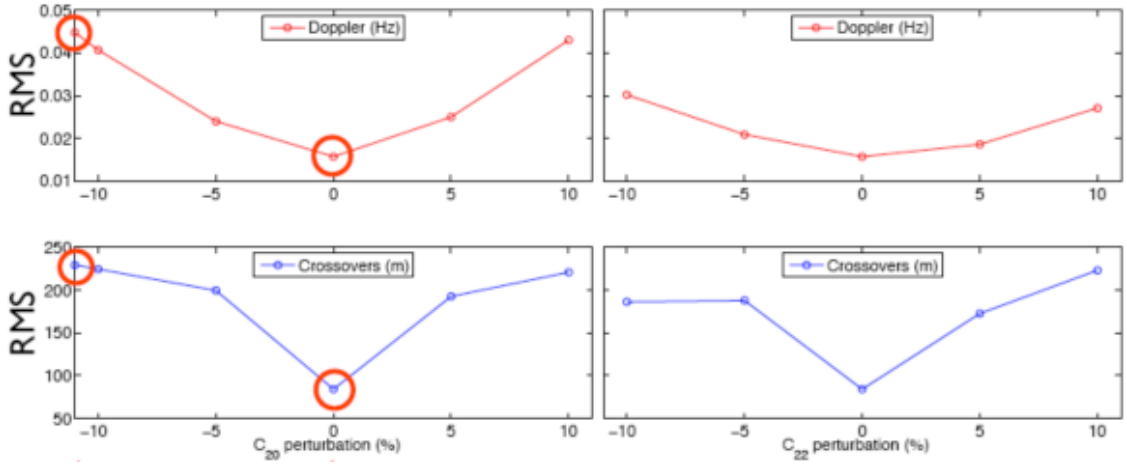

Figure S6. Validation of recovery of C_{20} (left) and C_{22} (right) from Doppler (top) and altimeter crossover (bottom) data in an arc using data between 9 March and 5 June 2011. The best-fit value for each coefficient, with corresponding minimum RMS residual, represents the zero-percent perturbation point along each abscissa. Perturbing the solution in either direction increases the RMS residual. The Doppler X-band residuals are expressed in Hz, and the altimeter crossover residuals are expressed in m.

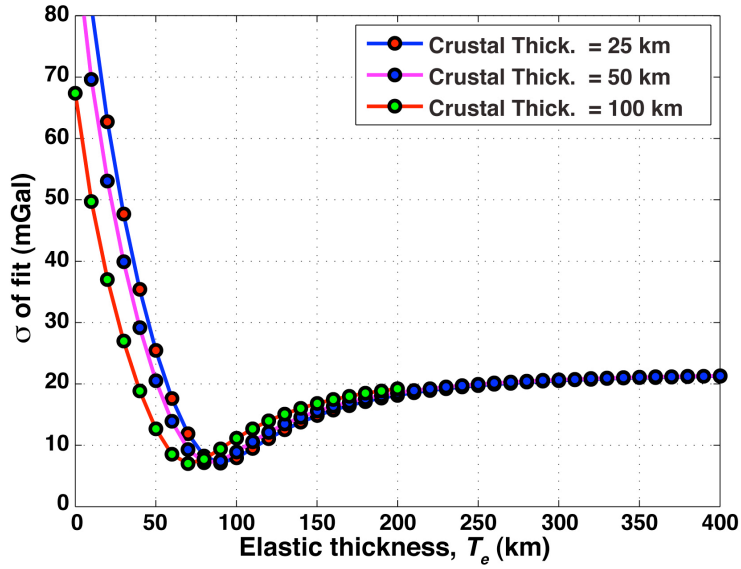

Figure S7. Standard deviation (σ) of the residuals from fits of the model gravity to HgM002 gravity in the vicinity of Mercury's northern rise. Results are shown for three different values of crustal thickness (h_c). The best fitting elastic lithosphere thicknesses are relatively insensitive to crustal thickness values.